

# 74 MHz Nonthermal Emission from Molecular Clouds: Evidence for a Cosmic Ray Dominated Region at the Galactic Center

F. Yusef-Zadeh<sup>1\*</sup>, M. Wardle<sup>2</sup>, D. Lis<sup>3</sup>, S. Viti<sup>4</sup>, C. Brogan<sup>5</sup>, E. Chambers<sup>6</sup>, M. Pound<sup>7</sup> & M. Rickert<sup>1</sup>

<sup>1</sup>*Department of Physics and Astronomy and Center for Interdisciplinary Research in Astronomy, Northwestern University, Evanston, IL 60208, USA*

<sup>2</sup>*Department of Physics & Astronomy, and Research Centre for Astronomy, Astrophysics & Astrophotonics, Macquarie University, Sydney NSW 2109, Australia*

<sup>3</sup>*California Institute of Technology, MC 320-47, Pasadena, CA 91125, USA*

<sup>4</sup>*Department of Physics and Astronomy, University College London, Gower St. London, WC1E 6BT, UK*

<sup>5</sup>*National Radio Astronomy Observatory, Charlottesville, VA 22903, USA*

<sup>6</sup>*University of Cologne, Cologne, Physikalisches Institut, Universität zu Köln, 50397, Germany*

<sup>7</sup>*University of Maryland, Department of Astronomy, College Park, MD 20742, USA*

## ABSTRACT

We present 74 MHz radio continuum observations of the Galactic center region. These measurements show nonthermal radio emission arising from molecular clouds that is unaffected by free-free absorption along the line of sight. We focus on one cloud, G0.13–0.13, representative of the population of molecular clouds that are spatially correlated with steep spectrum ( $\alpha_{327\text{MHz}}^{74\text{MHz}} = 1.3 \pm 0.3$ )

nonthermal emission from the Galactic center region. This cloud lies adjacent to the nonthermal radio filaments of the Arc near  $l \sim 0.2^\circ$  and is a strong source of 74 MHz continuum, SiO (2-1) and FeI  $K\alpha$  6.4 keV line emission. This three-way correlation provides the most compelling evidence yet that relativistic electrons, here traced by 74 MHz emission, are physically associated with the G0.13–0.13 molecular cloud and that low energy cosmic ray electrons are responsible for the FeI  $K\alpha$  line emission. The high cosmic ray ionization rate  $\sim 10^{-13} \text{ s}^{-1} \text{ H}^{-1}$  is responsible for heating the molecular gas to high temperatures and allows the disturbed gas to maintain a high velocity dispersion. LVG modeling of multi-transition SiO observations of this cloud implies  $\text{H}_2$  densities  $\sim 10^{4-5} \text{ cm}^{-3}$  and high temperatures. The lower limit to the temperature of G0.13-0.13 is  $\sim 100\text{K}$ , whereas the upper limit is as high as  $1000\text{K}$ . Lastly, we used a time-dependent chemical model in which cosmic rays drive the chemistry of the gas to investigate for molecular line diagnostics of cosmic ray heating. When the cloud reaches chemical equilibrium, the abundance ratios of HCN/HNC and  $\text{N}_2\text{H}^+/\text{HCO}^+$  are consistent with measured values. In addition, significant abundance of SiO is predicted in the cosmic ray dominated region of the Galactic center. We discuss different possibilities to account for the origin of widespread SiO emission detected from Galactic center molecular clouds.

*Subject headings:* astrochemistry - ISM: abundances—ISM: molecules—ISM: lines and bands

## 1. Introduction

The interstellar medium (ISM) of the nucleus of our Galaxy has unique characteristics. Gas clouds are subject to the strong tidal field of the nucleus and are required to have higher

density than in the Galactic disk in order to become gravitationally unstable and form stars. This region of the Galaxy hosts two components in its central few hundred parsec. One is the reservoir of molecular gas showing enhanced molecular emission with higher velocity dispersion ( $\sim 20 - 30$ ) km s<sup>-1</sup> and gas temperature (50-200K) compared to elsewhere in the rest of the Galaxy<sup>1-7</sup>. The other is the prevalence of a mixture of thermal emission from ionized gas at a temperature of few thousand degrees and nonthermal radio synchrotrone emission from relativistic electrons (e.g.; Nord et al. 2004; Law et al. 2008). The synchrotron emission is best viewed at low radio frequencies ( $< 1$ GHz) whereas thermal free-free emission is better detected at high frequencies ( $> 1$ GHz). Large-scale surveys of this region suggest that relativistic electrons and molecular gas co-exist and possibly interact with each other. However, the apparent correlation could result from chance coincidence along the long line of sight towards the Galactic center. We present the first evidence for low frequency nonthermal emission closely tracing molecular gas, establishing that cosmic ray electrons are physically associated with individual molecular clouds. We study one molecular cloud G0.13-0.13 in detail and postpone the discussion of other Galactic center clouds to elsewhere.

The interaction between cosmic-ray particles and molecular gas has several far reaching consequences. For one, cosmic rays play an important role in star formation processes as they are the primary source of ionization in molecular clouds that are self-shielded from UV radiation field. The interaction of cosmic ray electrons heats the gas to a higher temperature, which increases the Jeans mass and causes the initial mass function (IMF) to become top-heavy<sup>8-10</sup>. The higher ionization fraction due to the impact of these electrons reduces the damping of MHD waves and helps to maintains the high velocity dispersion of molecular gas in the nuclear disk. In addition, this interaction strengthens the coupling of gas to the magnetic field slowing star formation by increasing the time scale for ambipolar diffusion before the onset of gravitational collapse.

Recent measurements indicate a vast amount of  $\text{H}_3^+$  and  $\text{H}_3\text{O}^+$  <sup>11–14</sup> as well as high temperature molecular gas distributed in the Galactic center. The inferred minimum cosmic ray ionization rate,  $\zeta \sim 10^{-15} \text{ s}^{-1} \text{ H}^{-1}$ , is one to two orders of magnitude higher in the Galactic center region than in the Galactic disk<sup>10,13</sup>. The elevated cosmic ray ionization rate will increase the ionization fraction of electrons in molecular gas, and drive ion-neutral chemistry. Another consequence is enhanced fluorescent FeI  $K\alpha$  6.4 keV emission<sup>15,16</sup>. This nonthermal X-ray emission is uniquely detected from Galactic center clouds and results from filling the inner K-shell vacancies of neutral iron created by the impact of low energy cosmic ray electrons or by irradiation by X-ray photons<sup>17–20</sup>. A widely accepted model argues that the 6.4 keV line is a result of irradiation by a hypothetical transient source associated with Sgr A\*, which was active about 400 and again 100 years ago, and that we are seeing this transient’s light echo in the 6.4 keV emission<sup>21</sup>. We discuss another scenario in which low energy cosmic rays can contribute significantly in production of the FeI  $K\alpha$  line emission from Galactic center clouds.

The Galactic center population of molecular clouds have physical conditions similar to hot cores, but with the exception of Sgr B2, there is no strong evidence for ongoing massive star formation throughout the inner few hundred parsecs of the Galaxy, a region known as the central molecular zone (or CMZ)<sup>22</sup>. Line emission from a variety of molecular species has been detected throughout the CMZ including those that are produced in the gas phase (e.g.; HCN,  $\text{HCO}^+$ , HNC,  $\text{N}_2\text{H}^+$ ) as well as those processed on grain surfaces, e.g. SiO <sup>6,7</sup>. With the exception of the strong radiation field near Sgr A\* and the Arches cluster, PDRs can not be very important in the dense self-shielded clouds. In addition, the X-ray flux from the Galactic center is too weak to qualify for the application of XDR models. Global heating by cosmic rays can explain why the gas temperature is significantly higher than the dust temperature in a large fraction of the gas and dust clouds in the nuclear disk. In the cosmic-ray dominated region of the Galactic center, cosmic-ray heating should be more significant

than ambipolar and turbulent heating<sup>23</sup>. Thus, it is natural to examine the chemistry of the gas in the cosmic-ray dominated region and attempt to identify molecular line diagnostics of cosmic ray heating.

To this end, we present high resolution 74 MHz observations of the Galactic center and show the spatial correlation between molecular gas and 100 MeV cosmic ray electrons. Enhanced 74 MHz emission appears to coincide with a large concentration of molecular gas in the inner  $5^\circ$  of the Galactic center<sup>24</sup>. Here, we focus on G0.13–0.13, a representative molecular cloud, and compare its 74 MHz emission with that of excited rotational transitions of SiO and CS molecules. This molecular cloud lies along the nonthermal filaments of the radio Arc near  $l \sim 0.2^\circ$ , the most prominent network of magnetized filaments in the Galactic center. Molecular line emission from CO, CS, SiO,  $\text{H}^{13}\text{CO}^+$  and CS suggests that this cloud has a high column density and gas temperature<sup>25–27</sup>. The kinematics of CS line emission from G0.13–0.13 suggests an expansion of molecular gas into the nonthermal filaments<sup>25</sup>. CO observations imply gas temperature  $T \geq 70\text{K}$  and column density  $N(\text{H}_2) = 6\text{--}7 \times 10^{23} \text{ cm}^{-2}$ . Multiple transitions of  $\text{NH}_3$  line emission from this cloud have measured two temperature components giving a range  $T \sim 25\text{K}$  and  $T \sim 125\text{--}200\text{K}$ <sup>28</sup>. The low temperature component of molecular gas is similar to the measured 18–22 K dust temperature in clouds in the inner  $2^\circ \times 1^\circ$  of the Galaxy<sup>29,30</sup>.

The structure of this paper is as follows. We first show 74 MHz emission from Galactic center molecular cloud G0.13–0.13 and estimate the variation of spectral index of nonthermal emission between 327 and 74 MHz. We then show the association of the nonthermal radio emission from G0.13–0.13 with FeI  $K\alpha$  line emission at 6.4 keV and estimate the cosmic ray ionization rate needed to produce the FeI  $K\alpha$  line emission. We will also present new molecular line observations of four rotational transitions of SiO to determine the temperature and density of molecular gas in G0.13–0.13 more accurately. We consider the interaction

of relativistic electrons with the gas and compute the cosmic ray ionization rate, implied by the 74 MHz emission, as a function of assumed magnetic field strength. We present the dependence of the total cooling rate of the gas on gas temperature for high molecular gas densities. Lastly, we study the chemical consequences of the interaction of cosmic ray electrons with the molecular gas by modeling the abundance ratios of several molecular species as a function of time. A time-dependent gas-grain chemical model<sup>31</sup> is used to explore how abundance ratios of five representative molecular species vary with gas density and cosmic-ray ionization rate.

Our study of G0.13–0.13 is not only relevant to understanding the molecular component of the nuclear disk of our Galaxy<sup>8</sup> but also to external galaxies and ultraluminous infrared galaxies (ULIRGs) where cosmic rays are thought to be the driving mechanism for star formation<sup>9</sup>.

## 2. Observations and Data Reduction

We imaged the Galactic center at 74 MHz and mapped molecular line emission from several molecular clouds in the Galactic center using Mopra, CSO and CARMA. We only present observations of G0.13–0.13 here and will describe details of observations of other Galactic center clouds elsewhere.

### 2.1. VLA

The 74 MHz radio continuum observations of the Galactic center were described previously<sup>24</sup>. Briefly, these measurements were taken in multiple configurations of the Very Large Ar-

ray (VLA) of the National Radio Astronomy Observatory<sup>1</sup> (NRAO), with a resolution of  $114'' \times 60''$  (PA=  $-5^\circ$ ) and rms sensitivity of  $\sim 0.12$  Jy. These observations are unprecedented in spatial resolution and sensitivity at these low frequencies. Given the strong frequency dependence ( $\nu^{-2.1}$ ) of free-free absorption, foreground and embedded thermal sources are seen in absorption against the strong nonthermal emission from the Galactic center. The suppression of thermal emission due to high opacity of ionized gas at 74 MHz allows us to readily identify nonthermal sources that emit at this frequency.

## 2.2. CSO

Observations of the SiO (5–4) and (6–5) rotational transitions at 217.1 and 260.5 GHz, respectively, were carried out in 2010 September using the wideband 230 GHz “Z-Rx” receiver of the Caltech Submillimeter Observatory (CSO) on Mauna Kea, Hawaii. The weather conditions were good, characterized by a 225 GHz zenith opacity of  $\sim 0.05 - 0.07$ , equivalent to 1–1.5 mm of precipitable water vapor. Typical single sideband system temperatures at the relatively low elevation of the Galactic center were  $\sim 250$  K. The CSO FWHM beam size at the two frequencies is  $\sim 34''$  and  $28''$ , respectively, and the main beam efficiency, as determined from total power observations of Jupiter, was  $\sim 70\%$ . Spectra were taken in the “on-the-fly mapping” mode, on a  $\sim 15''$  grid, using a designated off position at  $(\alpha, \delta)_{2000.0} = (17^h 45^m 13.^s 2, -28^\circ 45' 31.'' 0)$ , out of the Galactic plane. Multiple maps scanned in orthogonal directions were averaged together to avoid striping. The final per pixel integration time (ON) was 14–17 sec for SiO 5–4 and 25–31 sec for SiO 6–5. We used the high-resolution CSO facility FFTS spectrometer with 8192 channels and a total bandwidth of 1 GHz.

---

<sup>1</sup>The National Radio Astronomy Observatory is a facility of the National Science Foundation, operated under a cooperative agreement by Associated Universities, Inc.

### 2.3. Mopra

We observed G0.13–0.13 on 2010, June 28 using Mopra<sup>2</sup> in the on-the-fly mapping mode. The map size is 5' by 5', and is centered at Galactic longitude and latitude (l, b)=(0.1092°, –0.1000°). We used a latitude scan direction (orthogonal to the Galactic plane), and a row spacing of  $\sim 15''$ . We used the MOPS spectrometer in Wideband mode, with a central frequency of 89.690 GHz. This results in a frequency coverage of  $\sim 85.6 - 93.8$ GHz across four sub-bands. Each sub-band has 8192 channels, a channel width of 269.5 kHz ( $\sim 0.9 \text{ km s}^{-1}$ ), and two linear polarizations. The final map is the average of the two polarizations. Regular pointing checks done throughout the observations, and were within  $\sim 4''$  (the beam size is  $\sim 38''$  at these frequencies). The intensity is given in  $T_A^*$  which can be divided by the main beam efficiency 0.49 to convert the intensity to  $T_{mb}$ .

We also made deep pointed observations toward four positions (A-D) within G0.13–0.13 on 2010, June 30 (see Table 1). These spectra were obtained in an on-off position switching mode for a total on-source time of 288 s. The MOPS spectrometer was configured in wideband mode, identically to the setup of the map described above. A total of 16 molecular lines CH<sub>3</sub>CN, C<sup>13</sup>CN, <sup>13</sup>CS, N<sub>2</sub>H<sup>+</sup>, HNC, HCCN, HNCO, HCN, HCO<sup>+</sup>, <sup>28</sup>SiO, HC<sup>15</sup>N, SO, H<sup>13</sup>CN, H<sup>13</sup>CO, SiO, NH<sup>15</sup>C and C<sub>2</sub>H are detected from four positions in G0.13–0.13 (see Fig. 7).

---

<sup>2</sup> The data was obtained using the Mopra radio telescope, a part of the Australia Telescope National Facility which is funded by the Commonwealth of Australia for operation as a National Facility managed by CSIRO. The University of New South Wales (UNSW) digital filter bank (the UNSW-MOPS) used for the observations with Mopra was provided with support from the Australian Research Council (ARC), UNSW, Sydney and Monash Universities, as well as the CSIRO.



## 2.4. BIMA

We mapped G0.13–0.13 in CS(2-1) at 97.980968 GHz and HCO<sup>+</sup>(1-0) at 89.188518 GHz with the Berkeley-Illinois-Maryland Association (BIMA) interferometer<sup>3</sup> during the 2002-2003 observing season. The BIMA array was a mm-wavelength interferometer located in Hat Creek, California<sup>32</sup>, consisting of ten 6.1 m antennas. These antennas have since been combined with the Owens Valley Radio Observatory 10 m antennas into the CARMA<sup>4</sup> millimeter array at Cedar Flat, California.

The cloud was observed with 20 mosaicked pointings on a hexagonal grid corresponding to Nyquist sampling of the primary beam and covering a total area of about 5' × 6'. The pointing center was  $(\alpha, \delta)_{2000.0} = (17^h 46^m 24.^s 0, -28^\circ 45' 00.'' 0)$  with a velocity of 30 km s<sup>-1</sup> with respect to the local standard of rest. The HCO<sup>+</sup> and CS data were obtained simultaneously in opposite sidebands. Each of the spectral lines were observed with a 50.0 MHz correlator window with 256 channels. Along with the spectral data, continuum windows with a total coverage of about 800 MHz were also observed. We observed in the C and B configuration of the array, sampling spatial frequencies from 1 to 78 kλ. Absolute flux calibration was derived from observations of Mars or Uranus immediately before or after the source track. The quasar 1733-130 was used as the phase calibrator and secondary flux calibrator. To fill the inner *uv* spacings, we also obtained fully-sampled maps covering the region imaged with the array in the HCO<sup>+</sup>, and CS using the Five Colleges Radio Astronomy Observatory 14 m telescope, as well as the previously published CS(2-1) maps made with Nobeyama 45-m radio telescope (NRO)<sup>25</sup>. A more detailed high resolution kinematic study

---

<sup>3</sup>The BIMA interferometer was operated under a joint agreement between the University of California, Berkeley, the University of Illinois, and the University of Maryland with support from the National Science Foundation.

<sup>4</sup>Combined Array for Research in Millimeter-wave Astronomy; <http://www.mmarray.org>

of G0.13–0.13 including the results of  $\text{HCO}^+$  observations will be given elsewhere.

### 3. Results

Figure 1a,b shows the distribution of 74 MHz continuum and the CO (3-2) line from the inner  $1.5^\circ \times 12'$  of the Galactic center. A layer of molecular gas in the CMZ runs parallel to the Galactic plane and is seen in the distribution of CO (3-2) line emission<sup>33</sup>. This layer includes some of the most prominent molecular clouds in the CMZ such as Sgr B2 and Sgr B1, the 40, 50, –30 and 20  $\text{km s}^{-1}$  Sgr A and Sgr C clouds. Some of the prominent clouds are labeled on Figures 1a,b. At positive longitudes, the Sgr B2 complex, G0.36-0.09 and G0.13–0.13 have 74 MHz counterparts and at negative longitudes the layer of molecular gas that runs parallel to the Galactic plane G359.75-0.23 shows a 74 MHz counterpart. Another presentation of the CO (3-2) and 74 MHz emission is shown in Figure 1c. The distribution of 74 MHz emission appears to follow the CO (3-2) line emission except in two types of regions. One type is associated with holes created by free-free absorption suppressing background 74 MHz emission and the other is where nonthermal continuum sources have no molecular counterparts. Overall, the 74 MHz emission shows similar morphology to that of CO (3-2) line emission apart from absorption features manifesting as holes in the 74 MHz distribution. To clarify the correlation between absorption features and free-free emission, Figure 1d presents a continuum map at 8.5 GHz based on GBT observations<sup>34</sup>. Prominent continuum sources are labeled on this figure. Holes in the 74 MHz continuum map coincide with strong continuum emission at 8.5 GHz, consistent with the free-free absorption coefficient increasing significantly at low frequencies. Thus, thermal sources become optically thick and are seen in absorption against strong nonthermal background emission<sup>35</sup> whereas nonthermal sources that are not contaminated by significant foreground thermal emission are clearly identified at 74 MHz. The morphological comparison of these figures suggest that

nonthermal continuum emission at 74 MHz arises from Galactic center molecular clouds, implying that cosmic-ray electrons are interacting with molecular gas in this unique region of the Galaxy.

We now focus on the G0.13–0.13 cloud. Figure 2a shows contours of CS (1-0) molecular line emission from this cloud superimposed on a grayscale 5 GHz continuum image. A network of linearly polarized filaments of the radio Arc running almost perpendicular to the Galactic plane at a  $PA \sim -170^\circ$  lies at the eastern edge of the cloud<sup>37</sup>. The morphology of molecular line and radio continuum emission from G0.13–0.13 suggests that the molecular gas is surrounded by, and is interacting with, nonthermal radio filaments. The kinematics of the molecular gas suggests that expansion of the cloud is responsible for a dynamical interaction between the eastern limb of the G0.13–0.13 and the magnetized nonthermal filaments<sup>25</sup>. Figure 2b shows high resolution CS (2-1) line emission from the G0.13–0.13 molecular cloud (red) superimposed on a 1.4 GHz continuum image (green). The molecular gas distribution is clumpy with the morphology of a “boot”, and is edge-brightened parallel to the nonthermal radio filaments of the Arc near  $l \sim 0.2^\circ$  on the eastern edge of the cloud. We note that the western edge of the cloud lies parallel to another magnetized nonthermal filament G0.087-0.087<sup>38</sup>. The molecular line images show a ridge of emission that deviated from a straight line perpendicular to the Galactic plane (labelled as “Meandering feature” on Figure 2a) near  $l \sim 8'$ ,  $b \sim -7'$ . This ridge of emission appears to curve around a nonthermal filament near  $l = 8' 4''$ ,  $b = -6' 55''$ . This high resolution map of molecular line emission provides the strongest morphological support for the interaction of the nonthermal filaments and the eastern edge of G0.13–0.13.

Figure 3a,b show contours of 74 and 327 MHz emission, respectively, superimposed on a grayscale image at 5 GHz. The 74 MHz emission is produced mainly by nonthermal processes whereas 5 GHz and 327 MHz emission can trace emission produced by both thermal and

nonthermal processes. The distribution of 74 MHz emission differs remarkably from the 327 MHz and 5 GHz continuum. The 74 MHz emission arises from the vertical filaments as well as the region where the G0.13–0.13 molecular cloud lies. There is no evidence of thermal emission from G0.13–0.13 at 327 MHz or at higher frequencies, thus, the spectrum derived here is not contaminated by thermal emission. The vertical filaments seen in the grayscale image at 5 GHz have counterparts at 74 MHz except in the thermal region to the north of the filaments near G0.18–0.04. This is because G0.18–0.04 is an HII region dominated by free-free emission at high frequencies, thus the lack of 74 MHz emission is due to significant free-free absorption<sup>35</sup>.

What is remarkable about images shown in Figure 3a,b is the discovery that enhanced nonthermal emission at 74 MHz arises from the molecular cloud G0.13–0.13. The spectrum of emission from the center of the cloud must be steep given that there is no strong 327 MHz emission from G0.13–0.13. Figure 3c shows the spectral index distribution (where the flux density  $F_\nu \propto \nu^{-\alpha}$ ) between 327 and 74 MHz. The spectrum is inverted ( $\alpha < 0$ ) at the position of the filaments and is steep ( $\alpha \sim 1.3$ ) where the molecular line and 74 MHz emission peak. There is no evidence of thermal emission from G0.13–0.13 at 327 MHz or at higher frequencies, thus, the spectrum derived here is not contaminated by thermal emission.

Another version of the spectral index distribution is made by comparing the background subtracted profiles of the emission at 74 and 327 MHz. Figures 3d,e show two different cross cuts made at constant longitude  $l=-6'$  and constant latitude  $b=-8'$ , respectively. This technique follows earlier work by Law et al. (2008). The spectral index distribution, as shown in Figure 3d, is consistent with a steep spectrum ( $\alpha = 1.1 \pm 0.2$ ) becoming flatter or inverted at the nonthermal vertical filaments. Figure 3e shows  $\alpha \approx -0.2 \pm 0.05$  between 74 and 327 MHz at the position of nonthermal filaments. The electron energy spectrum of the center of G0.13–0.13 is remarkably steep,  $p \approx 3.2$  (where  $p=2\alpha+1$  corresponding to energy

spectrum  $E^{-p}$ ). In contrast, the spectral index of the vertical filaments is remarkably flat  $p \approx 0.6$ . The variation of the spectral index of nonthermal emission from the filaments and G0.13–0.13, is  $\Delta\alpha \sim 1.5$ .

G0.13–0.13 is one of the Galactic center molecular clouds showing bright FeI  $K\alpha$  line emission at 6.4 keV<sup>39</sup>. Figure 4 shows contours of fluorescent FeI  $K\alpha$  line emission based on Chandra observations convolved to a resolution of  $30''$  and superimposed on a grayscale distribution of integrated CS (1-0) line emission. High resolution Chandra and CARMA images of this cloud show a clumpy distribution of  $K\alpha$  line emission<sup>20</sup> tracing CS (1-0) line emission. The overall distribution of FeI  $K\alpha$  line emission arising from G0.13–0.13 is similar to that of low frequency radio emission molecular line CS and SiO emission. The distribution of the  $K\alpha$  line emission is clumpy and shows a ridge of emission adjacent to a nonthermal feature at  $l=8' 10''$   $b=-6' 55''$ . Remarkably, this X-ray ridge feature is similar to that of CS emission (cf. Meandering feature in Fig. 2b). Both the X-ray and CS ridges curve around a nonthermal filament. The morphology of 6.4 keV line emission supports the idea that nonthermal radio filaments are interacting with the edge brightened FeI  $K\alpha$  emitting molecular cloud G0.13–0.13 at 6.4 keV. These images suggest a three-way correlation between cosmic ray electrons, molecular gas and FeI  $K\alpha$  line emission.

In order to estimate the gas density and temperature in G0.13–0.13, we measured the line intensities of four transitions of SiO (6-5), (5-4), (2-1) and (1-0). We used the SiO (1-0) and (2-1) images taken from Handa et al. (2006) and convolved them to the same resolution and velocity coverage, between -10 to 50 km s<sup>-1</sup> as those of SiO (6-5) and (5-4) transitions. Figure 5a shows contours of velocity integrated SiO (5-4) line emission mapped over a limited area of G0.13–0.13 superimposed on a 5 GHz continuum image. We applied a Large Velocity Gradient (LVG) model to the two E and NW rectangular boxes, as shown schematically, in order to derive the physical parameters of molecular gas in G0.13–0.13.

The LVG grid was computed for a constant SiO column density of  $1.6 \times 10^{13} \text{ cm}^{-2}$  and a line width of  $30 \text{ km s}^{-1}$ . This approximately reproduces the observed line intensities for the range of densities and temperatures applicable to the gas in the Galactic center region. With these assumptions, the emission is optically thin (typical optical depths ranging between 0.1 and  $10^{-3}$ , depending on the transition). Thus, optical depth effects do not influence the LVG model results as long as the beam filling factor is close to unity. A smaller beam filling factor will change the optically thin assumption we have made. Figure 5b,c show the density and kinetic temperature constraints estimated from three SiO line ratios of the E and NW boxes in three different colors, respectively. The three line ratios give a wider range of gas temperature between  $\approx 100 - 1000\text{K}$  for box E and  $\approx 400 - 1000\text{K}$  for box NW. A lower range of gas temperatures  $> 100\text{K}$  is found from the region near the nonthermal filaments of the Arc, box E as shown in Figure 5a, than that of the peak emission in the NW box having  $T > 400\text{K}$ . The implied kinetic temperatures are consistent with earlier measurements based on multiple transitions of  $\text{NH}_3$  <sup>28</sup>. Additional constraints have also been made by estimating molecular gas pressure from the NW box of Figure 5a. The top three panels of Figure 5d show the plots of line ratios for all models in the grid as function of logarithm of pressure ( $nT$ ). The bottom panel shows a sum of  $[(\text{model-observed})/\text{observed}]^2$  for the three line ratios and the best fit is obtained for  $\log(nT)$  in the range of 6.4–6.9. The line ratios give values of density and temperature that are consistent with  $\log(n) \sim 4.4$  and  $\log(T) \sim 2.3$  for minimum  $\chi^2$  values. Similar values were obtained for the E box of Figure 5a.

Tsuboi et al. (2011) used the SiO (2-1)/(1-0) line ratios to estimate a molecular gas density of  $\sim 10^4 \text{ cm}^{-3}$  at a kinetic temperature of 60K. On the other hand, Oka et al. (2001) used the CO (2-1)/(1-0) intensity ratios and argued that G0.13–0.13 has a low density  $\sim 10^2 \text{ cm}^{-3}$ , high kinetic temperature  $\geq 70\text{K}$  component. Overall, our model fits which uses multiple transitions of SiO are suited to measure gas density and temperature, though with systematic uncertainties from using different telescopes. The application of the LVG

excitation code constrains the gas density of hydrogen nuclei  $n_{\text{H}} \sim (1 - 3) \times 10^4 \text{ cm}^{-3}$  and temperature  $T \sim (1 - 2) \times 100\text{K}$  but we can not rule out gas temperature as much as 1000K and lower densities  $n \sim 10^3 \text{ cm}^{-3}$ .

Two studies have made discrepant estimates of the column density of the gas in G0.13–0.13 <sup>26,40</sup> Using kinetic temperature  $T_k=70\text{K}$ , Handa et al. (2006) used  $\text{H}^{13}\text{CO}^+$  (J=1-0) line emission which is expected to be optically thin with abundance of  $10^{-10}$  to derive an  $\text{H}_2$  column density  $(6-7) \times 10^{23} \text{ cm}^{-3}$ . On the other hand, Amo-Baladron et al. (2009) determined the physical condition by applying an LVG model to the SiO (2-1) and (3-2) transitions and then estimated the column of  $\text{H}^{13}\text{CO}^+$  (J=1-0). Using the same abundance as that of Handa et al. (2006), the derived column density of molecular hydrogen from this study is  $(2-8) \times 10^{22} \text{ cm}^{-3}$ . To resolve this discrepancy, we estimated the column density of molecular gas by using submillimeter emission from dust grains in G0.13–0.13. We used the data taken from Pierce-Price et al. (2000) who derived  $513 M_{\odot} \text{ Jy}^{-1} \text{ beam}^{-1}$  at  $850\mu\text{m}$  with the assumption that dust temperature is 20K, metallicity twice solar and opacity index  $\beta=2$ . Using background subtracted flux densities of 0.5 and 1.5 Jy from the NW and E boxes at  $850\mu\text{m}$  and a beam of  $15''$ , we find the column density of molecular hydrogen ranges between  $\sim 3.5 \times 10^{22}$  and  $\sim 10^{23}$ ,  $\text{cm}^{-2}$  respectively. There is uncertainty in accurately determining the background emission. Given this uncertainty, our estimate of the column density falls between previous measurements of Handa et al. (2006) and Amo-Baladron et al. (2009). Herschel maps presented by Molinari et al. (2011) give column density values that are consistent with our estimates.

#### 4. Discussion

Our interest in studying Galactic center molecular clouds stems from three earlier studies, all of which had suggested the interaction of cosmic ray electrons with molecular gas and

that cosmic ray electrons are enhanced in this region. First, fluorescent 6.4 keV  $K\alpha$  iron line emission from several molecular clouds in the Galactic center may be the consequence of the interaction of low energy cosmic ray electrons with molecular gas<sup>20,41</sup>, or alternatively, the irradiation of molecular clouds by a hypothetical X-ray flash associated with past activity of Sgr A\*<sup>21</sup>. Second, nonthermal bremsstrahlung from this electron population can also explain the diffuse  $\gamma$ -ray emission from the central  $2^\circ \times 1^\circ$  of the Galactic center<sup>42</sup>. Third, the strong  $H_3^+$  absorption along several lines of sight towards the Galactic center imply that the ionization rate is at least an order of magnitude higher than elsewhere in the Galaxy<sup>10</sup>. This is consistent with the low energy cosmic ray electron production of the FeI  $K\alpha$  line emission. Finally, low frequency diffuse radio emission<sup>43</sup> combined with spectral index measurements<sup>23</sup> suggest strong nonthermal continuum emission from the Galactic center. Our detailed study provides the most compelling evidence yet that relativistic electrons, here traced by 74 MHz emission, are physically associated with the G0.13–0.13 molecular cloud. This cloud is one of the strongest sources of FeI  $K\alpha$  line emission in the Galactic center. We complete our analysis by studying the complex morphology of G0.13–0.13, estimating the cosmic ray ionization rate, the expected FeI  $K\alpha$  line emission at 6.4 keV, and modeling chemical signature of the interaction.

#### 4.1. Morphology & Kinematics

G0.13–0.13 is a complex molecular cloud with kinematics that suggest expansion into the vertical filaments of the radio Arc<sup>25</sup>. Morphologically, this cloud lies at the center of a circular-shaped structure, known as the radio Arc bubble, apparent in mid-IR images taken with the Spitzer and MSX observatories<sup>44–47</sup>. Figure 6 shows contours of SiO (2-1) line emission, obtained with Mopra, superimposed on a three-color Spitzer IRAC image. The Arc bubble is noted exterior to the south of G0.13–0.13. The origin of the bubble and its



relation to the radio Arc and the G0.13–0.13 cloud is not well understood. Past studies have suggested that the radio Arc bubble lies in the vicinity of the Quintuplet star cluster and is produced by stellar winds or supernova explosions sweeping up interstellar material<sup>47</sup>. The nonthermal radio emission at 74 MHz and expansion of G0.13–0.13 point to the possibility that the Arc bubble may be produced by the same event. It is possible that an energetic event is driving a shock into G0.13–0.13. The shock reaches the edge of the cloud and before it encounters much lower density of the gas exterior to G0.13–0.13, then sweeps through the low density gas and creates a edge-brightened bubble. In this picture, the expansion of G0.13–0.13 into the nonthermal vertical filaments accelerates particles along the filaments<sup>25,48</sup>, thus generating a young population of electrons running along the magnetized filaments with an unusually flat energy spectrum ( $p \sim 0.6$ ). The puzzle, however, is the origin of the steep energy spectrum of particles with  $p > 3$  in G0.13–0.13. This is because energy losses are increasingly severe for lower energy electrons, tending to flatten their energy spectrum at low energies.

#### 4.2. Cosmic Ray Ionization Rate

Using equation (3) of Yusef-Zadeh et al. (2012), the cosmic ray ionization per second per hydrogen nucleus,  $\zeta$ , depends on the observed synchrotron intensity  $I_\nu$ , the magnetic field  $B$ , the depth of the source of emission along the line of sight,  $L$ , and the energy spectrum of the electrons with the index  $p$ , assumed to be power-law  $E^{-p}$  between 0.1 MeV and 1 GeV and  $\alpha = (p - 1)/2$  is the synchrotron spectral index and  $I_\nu \propto \nu^{-\alpha}$ .

$$\zeta \approx \frac{3.1 \times 10^{-14}}{p - 1} \frac{I_\nu}{\text{Jy arcmin}^{-2}} \left( \frac{\nu}{\text{GHz}} \right)^\alpha \left( \frac{L}{30 \text{ pc}} \right)^{-1} \left( \frac{B}{100 \mu\text{G}} \right)^{-(1+\alpha)} \text{ s}^{-1} \text{ H}^{-1} \quad (1)$$

Figure 7a shows the inferred cosmic ray ionization rate as a function of the magnetic

field strength for different values of  $\alpha$ . We assumed that  $L \sim 2.5$  pc ( $1'$  corresponds to 2.4pc at the Galactic center distance 8.5 kpc) and the observed surface brightness of 0.71 Jy arcmin<sup>-2</sup> at 74 MHz averaged over the inner  $5' \times 5'$  of G0.13–0.13. The black dot on the curve gives the equipartition magnetic field for the electron population producing diffuse synchrotron emission in the dense molecular cloud G0.13–0.13. The ionization rate due to electrons increases for steeper spectral index values for a fixed emissivity at the observed frequency, as there is a successively larger population of lower-energy electrons radiating at lower frequencies. The equipartition magnetic field ranges between 30  $\mu$ G and 0.3 mG for  $\alpha$  values between 0.25 to 1.5. The corresponding  $\zeta$  is estimated to be  $\sim 4 \times 10^{-15}$  and  $10^{-11}$  s<sup>-1</sup>, respectively. A cosmic ray ionization rate  $\geq 10^{-13}$  s<sup>-1</sup> H<sup>-1</sup> is sufficient to fully dissociate the gas on a time scale of  $\leq 10^6$  years. To avoid this, the magnetic field has to be larger than 1mG for  $\alpha = 1.25$ .

### 4.3. The 6.4 keV Neutral Iron Line Emission

We apply the cosmic ray model to the G0.13–0.13 molecular cloud by estimating the K $\alpha$  line emission from the interaction of the low energy nonthermal electrons responsible for synchrotron radio emission detected at 74 MHz. Using equation (6) of Yusef-Zadeh et al. (2012),

$$I_{K\alpha} \approx 8.7 \times 10^{-8} \left( \frac{\zeta}{10^{-14} \text{ s}^{-1}} \right) \left( \frac{N_{\text{H}}}{10^{23} \text{ cm}^{-2}} \right) \text{ ph s}^{-1} \text{ cm}^{-2} \text{ arcmin}^{-2}, \quad (2)$$

for  $N(\text{H}_2) = (1 - 3) \times 10^{23} \text{ cm}^{-2}$ , then the cosmic ray ionization rate needed to give the background subtracted K $\alpha$  line flux of  $3 \times 10^{-6} \text{ ph cm}^{-2} \text{ s}^{-1} \text{ arcmin}^{-2}$  derived from Suzaku observations<sup>39</sup> is  $\zeta \sim (1 - 3) \times 10^{-13} \text{ s}^{-1}$ , respectively. A value of cosmic ray ionization rate  $\zeta \sim 10^{-13} \text{ s}^{-1}$  is indicated by a dashed line on Figure 7a. Using the spectral index values between  $\alpha = 1$  and 1.25 and the gas density between few times  $10^{4-6} \text{ cm}^{-3}$ , the magnetic field strength is constrained to values between  $\sim 0.5$  and 1 mG, respectively.

A widely accepted alternative model argues that the 6.4 keV FeI  $K\alpha$  line emission results from irradiation of molecular clouds near the Galactic center by a hypothetical transient source associated with Sgr A\*, which was active about 400 and again 100 years ago<sup>21</sup>. The variability of 6.4 keV line emission on a short time scale provided a strong evidence in support of this hypothesis. However, the evidence for nonthermal emission from molecular clouds, as presented here, also predicts time variability in the context of the cosmic ray picture<sup>42</sup>. A supernova event expanding inside the cloud could change not only the ionization characteristics of the molecular gas in G0.13–0.13 but also causes the observed 6.4 keV time variability. Thus, the time variability of  $K\alpha$  line emission need not be clear support for the X-ray irradiation model.

#### 4.4. Cosmic Ray Heating of Molecular Gas

To estimate the temperature of molecular gas subject to high levels of cosmic-ray ionization, we extended our previous estimates of the cooling rate<sup>42</sup> to higher densities, using the fitting formula for cooling by rotational transitions of CO, H<sub>2</sub>, and H<sub>2</sub>O provided by Neufeld & Kaufman (1993) and Neufeld, Lepp & Melnick (1995). We also included an LVG calculation of the contribution by OI fine-structure lines, using the atomic data and collision rates in the Leiden Atomic and Molecular Database<sup>49</sup>. We adopted an abundance of CO relative to H<sub>2</sub> of  $2.8 \times 10^{-4}$ , twice the values adopted by Neufeld, Lepp & Melnick (1995) to reflect the higher metallicity of the gas in the CMZ. The abundance of OI and H<sub>2</sub>O is temperature-dependent because of the conversion of OI and O<sub>2</sub> to H<sub>2</sub>O by neutral-neutral reactions at temperatures above 200 K, so we assume twice the chemical equilibrium abundances of OI and H<sub>2</sub>O found by Neufeld, Lepp & Melnick (1995):  $\text{OI}/\text{H}_2 = 2 \times 10^{-4}/(1 + (T/220 \text{ K})^{14})$ , and  $\text{H}_2\text{O}/\text{H}_2 = \text{dex}(-6.222 + 2.831/(1 + (245\text{K}/T)^{14}))$ . We adopted a cloud column of  $2 \times 10^{23} \text{ H}_2 \text{ cm}^{-2}$  and a line FWHM  $20 \text{ km s}^{-1}$ .

The resulting total cooling rate per H<sub>2</sub> molecule is plotted in Figure 7b for representative H<sub>2</sub> densities of 10<sup>3</sup>, 10<sup>4</sup> and 10<sup>5</sup> cm<sup>-3</sup>. The cooling rates on the left hand axis are mapped to the right-hand axis showing the cosmic ray ionization rate that would supply heat at the same rate, assuming that each ionization is associated with the deposition of 12.4 eV of heat<sup>42,52</sup>. The dip in the cooling rate at  $T \approx 250$  K is due to the increasing importance of OI and H<sub>2</sub>O cooling at higher densities and the switch from OI to H<sub>2</sub>O at this temperature. We conclude that an ionization rate of 10<sup>-14</sup> to 10<sup>-13</sup> s<sup>-1</sup> would yield gas temperatures in the range 50–200 K, the upper range consistent with the temperatures estimated using LVG shown in Figure 5b,c.

#### 4.5. High Velocity Dispersion of Molecular Clouds

High cosmic-ray fluxes in molecular clouds affect star formation by heating the gas and increasing its ionization fraction. Higher cloud temperatures increase the Jeans mass, potentially changing the IMF, while high ionization increases magnetic coupling to the cloud material, reducing ambipolar diffusion and increasing the time taken for gravitationally unstable cores to contract to the point that they overwhelm their magnetic support. Another consequence of increased ionization is the therefore reduced damping of MHD waves, contributing to sustaining Alfvénic velocity fields within the clouds, which may assist in explaining the observed high velocity dispersion of molecular clouds in the nuclear disk (e.g. Oka et al. 1998; Martin et al. 2004). In a weakly ionized medium, waves with frequencies  $\omega \sim kv_A$  below the collision frequency of neutral particles with ions,  $\nu_{ni} = n_i \langle \sigma v \rangle$ , are damped on a time scale  $2\nu_{ni}/\omega^2$ <sup>53,54</sup> directly proportional to  $n_i$  which is increased by a factor of  $\sim 100$  compared to the Galactic disk for  $\zeta \sim 10^{-13}$  s<sup>-1</sup>. The power input required to maintain wave motions on a given scale is reduced by the same factor.

#### 4.6. Molecular Line Spectra toward G0.13–0.13

Figure 8a-d show line emission from 16 molecular lines toward four positions in G0.13–0.13 corresponding to A to D in Table 1, respectively. The spectra of these pointed observations show a rich chemistry similar to that seen throughout the CMZ. We focus only on five molecular lines HCN (1–0), HCO<sup>+</sup>(1–0), HNC(1–0), N<sub>2</sub>H<sup>+</sup>(1–0) and SiO (2–1), as Table 2 show the peak velocities and peak intensities in T<sub>A</sub><sup>\*</sup> of all five spectral lines. Positions A and D fall in the E and NW boxes (see Fig. 5a). As a demonstration, the spectrum of these five molecular species toward position A is shown in Figure 9. The strong velocity component associated with G0.13-0.13 is centered around 60 km s<sup>-1</sup> (see Table 2). We also notice an additional weak velocity component between -50 km s<sup>-1</sup> and 0 km s<sup>-1</sup>.

Using RADEX<sup>5</sup> (van der Tak et al. 2007)<sup>55</sup>, we derived the column density of each molecular species to match the observed intensity with the assumption that molecular gas temperature and gas density are T= 200 K and 10<sup>4</sup> cm<sup>-3</sup>, respectively and the velocity dispersion is 30 km s<sup>-1</sup>. Table 3 shows the log of column density ratio of HCN/HNC, HCO<sup>+</sup>/N<sub>2</sub>H<sup>+</sup> and SiO/N<sub>2</sub>H<sup>+</sup> in columns 2-4 and the corresponding antenna temperature ratios in column 5-8 based on deep Mopra observations at the four positions A-D given column 1. Calibration uncertainties of 25% have not been included in tables 2 and 3. We note that position C lies at the center of the boot-shaped structure, cf. Fig. 2b, where the 74 MHz emission peaks, implying that the cosmic ray ionization rate is higher than the other three positions.

---

<sup>5</sup><http://www.sron.rug.nl/~vdtak/radex/index.shtml>

#### 4.7. Chemical Modelling

To examine the effect of high cosmic-ray ionization rates on chemistry, we make use of a time-dependent gas-grain chemical model, UCL\_CHEM<sup>31</sup> to qualitatively investigate the behavior of the observed species. The UCL\_CHEM is a gas-grain time-dependent model; for the purpose of this paper it is used as a two-stage model: Phase I follows the free fall collapse of a diffuse ( $10^2 \text{ cm}^{-3}$ ) gas to a denser state (where the final density is a free parameter), while Phase II follows the chemistry as the gas and dust warm up due to either the increase of temperature and/or an enhanced cosmic ray ionization rate (Phase II). Apart from the very initial diffuse state (where the temperature is about 100K), during the collapse in Phase I the (coupled) gas and dust temperature remains constant at 10 K and atoms and molecules collide with, and freeze on to, grain surfaces. The advantage of this approach is that the ice composition is **not** assumed but it is derived by a time-dependent computation of the chemical evolution of the gas–dust interaction process which, in turns, depends on the density of the gas. Hydrogenation occurs rapidly on these surfaces, so that, for example, some percentage of carbon atoms accreting will rapidly become frozen out methane, CH<sub>4</sub>. The justification for a constant 10 K during most of Phase I is two-fold: first, in order for a diffuse gas to collapse under gravity and form a dense core, the temperature must remain low. Second, it is believed that methanol must form on icy mantles (and this implies an efficient freeze out of CO which can only occur for dust temperatures less than 20K) since experiments show that it can not form in the gas phase<sup>56</sup> (e.g., Geppert et al. 2006). In Phase II (which effectively represents the observed phase) the gas and dust temperature are decoupled; the temperature of the gas is varied from 50 to 200 K, while the dust temperature was kept to 20–30K. We employ the reaction rate data from the UMIST astrochemical database, augmenting it with grain-surface (hydrogenation) reactions<sup>31,57</sup> In both Phases nonthermal desorption is also considered<sup>58</sup>.

Figure 10 shows the abundance ratios of selected species as a function of time for a subset of our model grid where the final density was varied from  $10^4 \text{ cm}^{-3}$  to  $10^6 \text{ cm}^{-3}$  and the cosmic ray ionization rate from  $10^{-15} \text{ s}^{-1}$  to  $10^{-13} \text{ s}^{-1}$ . The gas temperature in Phase II was assumed to be  $\sim 200\text{K}$ . Note, however, that while molecular ratios are in principle powerful tools in constraining the physical and chemical characteristics of a cloud, the assumption that all the selected species arise from the same region may well be incorrect. Nevertheless, we assume that the selected species are co-spatial and consider a comparison between the theoretical column density ratios with those derived from our observations (see Table 3). The  $[\text{HCN}/\text{HNC}]$  (black) and  $[\text{HCO}^+/\text{N}_2\text{H}^+]$  (green) values, as drawn on the top right panel in dashed lines, agree with models of low density ( $10^4 \text{ cm}^{-3}$ ) and high cosmic ray ionization rate  $\zeta = 10^{-13} \text{ s}^{-1} \text{ H}^{-1}$ . We note an increase in the gas density and or a decrease in the cosmic ray ionization rate does not change the abundance ratio  $[\text{HCN}/\text{HNC}]$  but increases the  $\text{HCO}^+/\text{N}_2\text{H}^+$  (green) ratio to values well above the observed range of 0.005 to 0.19 of Table 3. The cosmic ray ionization rate, inferred independently from this model, is remarkably similar to that estimated from FeI  $K\alpha$  line measurements (see Fig. 7a). In addition, the gas density predicted from this chemical model is consistent within the range of values inferred from LVG models, as shown in Figure 5b,c.

It is known that Galactic center molecular clouds have high abundance of  $\text{SiO}^{59,60,61}$ . In one estimate, Minh et al. (1992) find the  $\text{SiO}$  abundance relative to molecular hydrogen to be between  $\sim 10^{-7}$  and  $10^{-8}$ . In other studies, Martin Pintado et al. (1997) also find a high abundance of  $\text{SiO} \sim 10^{-9}$  toward Galactic center molecular clouds. The observed  $[\text{SiO}/\text{N}_2\text{H}^+]$  abundance ratio ranges between 0.27–0.44 and can not be matched by any model at late enough times that chemical equilibrium has been reached. The models predict even higher fractional abundance of  $[\text{SiO}/\text{N}_2\text{H}^+]$ . In our models, we used an initial atomic abundance for Si depleted by a factor of 100 with respect to solar, as this represents the lower limit of measured initial abundances in a large sample of molecular clouds<sup>62</sup>. However,

all initial abundances<sup>63</sup> are then scaled to match a metallicity twice the solar value. Note that the abundance of SiO derived by our models is consistent with the fact that with high cosmic ray ionization rates the icy mantles are released and therefore Si is released in the gas phase. It is therefore puzzling to observe such a low fractional abundance in a gas where we expect cosmic ray ionization rates to be enhanced. There are three possibilities that could account for the low fractional abundance of  $[\text{SiO}/\text{N}_2\text{H}^+]$  compared to that predicted by chemical model. One is that the medium is quite turbulent and hence chemical equilibrium is never reached and the gas is constantly being recycled; then the best solution must be found at earlier times ( $< 10^4$  years). In this scenario all ratios can be qualitatively matched for the range of densities  $10^{4-5} \text{ cm}^{-3}$  and the whole range of cosmic ray ionization rates investigated and no further constraints can be given by the models. The other is that the initial atomic abundance of Si is low. Although we already employ, in models shown in Figure 10, an abundance of the initial Si  $1.64 \times 10^{-7}$  that is up to a factor of 100 depleted with respect to solar<sup>64</sup>. It could be that in these environments even more than a factor of 100 is depleted. Lastly, it is possible that our derivation of the column density from SiO (2-1) intensity is not accurate, e.g. optically thick. Thus, the intensity of high rotational transitions are needed to determine accurately the SiO column density. Additional detailed work is needed to sort out the discrepancy between the observed and modeled  $[\text{SiO}/\text{N}_2\text{H}^+]$  abundance ratio. What is clear from our chemical modeling, as in shocks and PDRs, a high SiO can also be generated by cosmic rays.

#### 4.8. Summary

We showed that the molecular emission from a Galactic center cloud G0.13-0.13, a representative molecular cloud in the CMZ, coincides with 74 MHz and FeI  $K\alpha$  line emission at 6.4 keV. This three-way correlation provides compelling evidence that relativistic electrons



are physically associated with the G0.13–0.13 molecular cloud. The high cosmic ray electron ionization rate  $\sim 10^{-13} \text{ s}^{-1} \text{ H}^{-1}$  is responsible for the FeI  $K\alpha$  line emission, heating the gas clouds to high temperatures and maintaining the velocity dispersion of clouds by increasing the wave damping time scale. One of the important conclusions of this study is that LVG modeling of multi-transition SiO observations gave molecular gas densities  $\sim 10^{4-5} \text{ cm}^{-3}$  and temperature  $\sim 100 - 1000\text{K}$ . The variation of the spectral index of nonthermal emission from G0.13-0.13 was shown to be unusually large  $\Delta\alpha \sim 1.5$ . We suggested that the expansion of the G0.13–0.13 molecular cloud into nonthermal vertical filaments accelerates particles along the filaments<sup>25,48</sup>, thus producing a young population of electrons with an unusually flat energy spectrum.

Evidence for FeI  $K\alpha$  line and 74 MHz synchrotron emission from warm molecular gas supports the view that the Galactic center is a cosmic ray dominated region. We explored the chemistry in a region subject to high levels of cosmic ray ionization and showed that enhanced SiO emission, widespread throughout Galactic center molecular clouds, can be produced in the context of cosmic ray interaction with molecular gas. The model to explain enhanced SiO, as well as  $\text{NH}_3$  and  $\text{CH}_3\text{OH}$ , emission by cosmic ray driven chemistry is an alternative to the shock-driven chemistry throughout Galactic center molecular clouds.

This research is supported in part by grants from the *Fermi* Guest Investigator Program as well as the grant AST-0807400 from the NSF the National Science Foundation. The Caltech Submillimeter Observatory is operated by the California Institute of Technology under cooperative agreement with the National Science Foundation (AST-0838261). Any opinions, findings, and conclusions or recommendations expressed in this material are those of the author(s) and do not necessarily reflect the views of the National Science Foundation.

## REFERENCES

- (1) Bally, J.; Stark, A.A.; Wilson, R.W.; Henkel, C. Galactic Center Molecular Clouds. II - Distribution and Kinematics. *Astrophys. J.* **1988**, *324*, 223-247
- (2) Dahmen, G.; Huttemeister, S.; Wilson, T. L.; Mauersberger, R.; Linhart, A.; Bronfman, L.; Tieftrunk, A. R.; Meyer, K.; Wiedenhoefer, W.; Dame, T. M. et al. Molecular gas in the Galactic Center Region. I. Data from a Large Scale C<sup>18</sup>O(J = 1–0) Survey. *Astron. Astrophys., Suppl. Ser.* **1997**, *126*, 197-236
- (3) Oka, T.; Hasegawa, T.; Sato, F.; Tsuboi, M.; Miyazaki, A. A Large-Scale CO Survey of the Galactic Center. *Astrophys. J., Suppl. Ser.* **1998**, *118*, 455-515
- (4) Martin, C. L.; Walsh, W. M.; Xia, K.; Lane, A. P.; Walker, C. K.; Stark, A. A. The AST/RO Survey of the Galactic Center Region. I. The Inner 3 Degrees. *Astrophys. J., Suppl. Ser.* **2004**, *150*, 239-262
- (5) Tsuboi, M.; Handa, T.; Ukita, N. Dense Molecular Clouds in the Galactic Center Region. I. Observations and Data. *Astrophys. J., Suppl. Ser.* **1999**, *120*, 1-39
- (6) Riquelme, D.; Bronfman, L.; Mauersberger, R.; May, J.; Wilson, T. L. A Survey of the Galactic Center Region in HCO<sup>+</sup>, H<sup>13</sup>CO<sup>+</sup>, and SiO. *Astron. Astrophys.* **2010**, *523*, A45
- (7) Jones, P. A.; Burton, M. G.; Cunningham, M. R.; Requena-Torres, M. A.; Menten, K. M.; Schilke, P.; Belloche, A.; Leurini, S.; Martin-Pintado, J.; Ott, J.; et al. Spectral Imaging of the Central Molecular Zone in Multiple 3-mm Molecular Lines. *Mon. Not. R. Astron. Soc.* **2012**, *419*, 2961-2986
- (8) Yusef-Zadeh, F.; Wardle, M.; Roy, S. Cosmic-Ray Heating of Molecular Gas in the Nuclear Disk: Low Star Formation Efficiency. *Astrophys. J.* **2007**, *665*, L123

- (9) Papadopoulos, P. P. A Cosmic-ray-dominated Interstellar Medium in Ultra Luminous Infrared Galaxies: New Initial Conditions for Star Formation. *Astrophys. J.* **2010**, *720*, 226-232
- (10) Oka, T.; Geballe, T. R.; Goto, M.; Usuda, T.; McCall, B. J. Hot and Diffuse Clouds near the Galactic Center Probed by Metastable  $H^+_{31}$ . *Astrophys. J.* **2005**, *632* 882-893
- (11) Goto, M.; Usuda, T.; Nagata, T.; Geballe, T. R.; McCall, B. J.; Indriolo, N.; Suto, H.; Henning, T.; Morong, C. P.; Oka, T. Absorption Line Survey of  $H^+_{31}$  toward the Galactic Center Sources. II. Eight Infrared Sources within 30 pc of the Galactic Center. *Astrophys. J.* **2008**, *688*, 306-319
- (12) Goto, M.; Usuda, T.; Geballe, T. R.; Indriolo, N.; McCall, B. J.; Henning, T.; Oka, T. Absorption-Line Survey of  $H_3^+$  toward the Galactic Center Sources. III. Extent of Warm and Diffuse Clouds. *Publ. Astron. Soc. Jpn.* **2011**, *63*, L13-L17
- (13) van der Tak, F.F.S.; Belloche, A.; Schilke, P.; Güsten, R.; Philipp, S.; Comito, C.; Bergman, P.; Nyman, L.-A. APEX Mapping of  $H_3O^+$  in the Sgr B2 Region. *Astron. Astrophys.* **2006**, *454*, L99-L102
- (14) Lis, D. C.; Carlstrom, J. E. Submillimeter Continuum Survey of the Galactic Center. *Astrophys. J.* **1994**, *424*, 189-199
- (15) Koyama, K.; Maeda, Y.; Sonobe, T.; Takeshima, T.; Tanaka, Y.; Yamauchi, S. ASCA View of Our Galactic Center: Remains of Past Activities in X-Rays?. *Publ. Astron. Soc. Jpn.* **1996**, *48*, 249-255
- (16) Murakami, H.; Koyama, K.; Maeda, Y. Chandra Observations of Diffuse X-Rays from the Sagittarius B2 Cloud. *Astrophys. J.* **2001**, *558*, 687-692

- (17) Sunyaev, R.; Churazov, E. Equivalent Width, Shape and Proper Motion of the Iron Fluorescent Line Emission from Molecular Clouds as an Indicator of the Illuminating Source X-ray Flux History. *Mon. Not. R. Astron. Soc.* **1998**, *297*, 1279-1291
- (18) Koyama, K.; Inui, T.; Matsumoto, H.; Tsuru, T. G. A Time-Variable X-Ray Echo: Indications of a Past Flare of the Galactic-Center Black Hole. *Publ. Astron. Soc. Jpn.* **2008**, *60*, S201-S206
- (19) Valinia, A.; Tatischeff, V.; Arnauld, K.; Ebisawa, K.; Ramaty, R. On the Origin of the Iron K Line in the Spectrum of The Galactic X-Ray Background. *Astrophys. J.* **2000**, *543*, 733-739
- (20) Yusef-Zadeh, F.; Law, C.; Wardle, M. The Origin of X-Ray Emission from a Galactic Center Molecular Cloud: Low-Energy Cosmic-Ray Electrons. *Astrophys. J.* **2002**, *568*, L121-L125
- (21) Ponti, G.; Terrier, R.; Goldwurm, A.; Belanger, G.; Trap, G. Discovery of a Superluminal Fe K Echo at the Galactic Center: The Glorious Past of Sgr A\* Preserved by Molecular Clouds. *Astrophys. J.* **2010**, *714*, 732-747
- (22) Morris, M.; Serabyn, E. The Galactic Center Environment. *Annu. Rev. Astron. Astrophys.* **1996**, *34*, 645-702
- (23) Li, P. S.; Myers, A.; McKee, C. Ambipolar Diffusion Heating in Turbulent Systems. *Astrophys. J.* **2012**, *760*, 33
- (24) Brogan, C. L.; Nord, M.; Kassim, N.; Lazio, J.; Anantharamaiah, K. Spatially Resolved Very Large Array 74 MHz Observations Toward the Galactic Center. *Astron. Nachr. Suppl.*, **2003**, *324*, 17-24

- (25) Tsuboi, M.; Ukita, N.; Handa, T. An Expanding Shell-like Molecular Cloud near the Galactic Center Arc. *Astrophys. J.* **1997**, *481*, 263
- (26) Handa, T.; Sakano, M.; Naito, S.; Hiramatsu, M.; Tsuboi, M. Thermal SiO and H<sup>13</sup>CO<sup>+</sup> Line Observations of the Dense Molecular Cloud G0.11-0.11 in the Galactic Center Region. *Astrophys. J.* **2006**, *636*, 261-266
- (27) Tsuboi, M.; Tadaki, K.; Miyazaki, A.; Handa, T. Sagittarius A Molecular Cloud Complex in H<sup>13</sup>CO<sup>+</sup> and Thermal SiO Emission Lines. *Publ. Astron. Soc. Jpn.* **2011**, *63*, 763-794
- (28) Hüttemeister, S.; Wilson, T.L.; Banina, T.M.; Martin-Pintado, J. Kinetic Temperatures in Galactic Center Molecular Clouds. *Astron. Astrophys.* **1993**, *280*, 255-267
- (29) Pierce-Price, D.; Richer, J. S.; Greaves, J. S.; Holland, W. S.; Jenness, T.; Lasenby, A. N.; White, G. J.; Matthews, H. E.; Ward-Thompson, D.; Dent, W. R. F.; et al. A Deep Submillimeter Survey of the Galactic Center. *Astrophys. J.* **2000**, *545*, L121-L125
- (30) Molinari, S.; Bally, J.; Noriega-Crespo, A.; Compiègne, M.; Bernard, J. P.; Paradis, D.; Martin, P.; Testi, L.; Barlow, M.; Moore, T.; et al. A 100 pc Elliptical and Twisted Ring of Cold and Dense Molecular Clouds Revealed by Herschel Around the Galactic Center. *Astrophys. J.* **2011**, *735*, L33
- (31) Viti, S.; Collings, M. P.; Dever, J. W.; McCoustra, M. R. S.; Williams, D. A. Evaporation of Ices Near Massive Stars: Models Based on Laboratory Temperature Programmed Desorption Data. *Mon. Not. R. Astron. Soc.* **2004**, *354*, 1141-1145
- (32) Welch, W. J.; Thornton, D. D.; Plambeck, R. L.; Wright, M. C. H.; Lugten, J.; Urry, L.; Fleming, M.; Hoffman, W.; Hudson, J.; Lum, W. T.; et al. The Berkeley-Illinois-Maryland-Association Millimeter Array. *Publ. Astron. Soc. Pac.* **1996**, *108*, 93

- (33) Oka, T.; Nagai, M.; Kamegai, K.; Tanaka, K.; Kuboi, N. A CO J = 3-2 Survey of the Galactic Center. *Publ. Astron. Soc. Jpn.* **2007**, *59*, 15-23
- (34) Law, C. J.; Yusef-Zadeh, F.; Cotton, W. D.; Maddalena, R. J. Green Bank Telescope Multiwavelength Survey of the Galactic Center Region. *Astrophys. J., Suppl. Ser.* **2008**, *177*, 255-274
- (35) Nord, M.E.; Lazio, T.J.W.; Kassim, N.E.; Hyman, S.J.; LaRosa, T.N.; Brogan, C.L.; Duric, N. High-Resolution, Wide-Field Imaging of the Galactic Center Region at 330 MHz. *Astron. J.* **2004**, *128*, 1646-1670
- (36) Camilo, F.; Ransom, S. M.; Gaensler, B. M.; Lorimer, D. R. Discovery of the Energetic Pulsar J1747-2809 in the Supernova Remnant G0.9+0.1. *Astrophys. J.* **2009**, *700*, L34-L38
- (37) Yusef-Zadeh, F.; Morris, M. G0.18-0.04 - Interaction of Thermal and Nonthermal Radio Structures in the Arc Near the Galactic Center. *Astron. J.* **1987**, *94*, 1178-1184
- (38) Reich, W. G0.087-0.087, A Highly Polarized Flat Spectrum Filament Near the Galactic Centre Arc. *Astron. Astrophys.* **2003**, *401*, 1023-1026
- (39) Uchiyama, H.; Nobukawa, M.; Tsuru, T.; Koyama, K.; Matsumoto, H. Global Distribution of Fe K $\alpha$  Lines in the Galactic Center Region Observed with the Suzaku Satellite. *Publ. Astron. Soc. Jpn.* **2011**, *63*, S903-S911
- (40) Amo-Baladron M. A.; Martin-Pintado, J.; Morris, M. R.; Munoz, M. P.; Rodriguez-Fernandez, N. J. SiO Emission as a Tracer of X-Ray Dominated Chemistry in the Galactic Center. *Astrophys. J.* **2009**, *694*, 943-950
- (41) Yusef-Zadeh, F.; Munoz, M.; Wardle, M.; Lis, D.C. The Origin of Diffuse X-Ray and

- $\gamma$ -Ray Emission from the Galactic Center Region: Cosmic-Ray Particles. *Astrophys. J.* **2007**, *656*, 847-869
- (42) Yusef-Zadeh, F.; Hewitt, J. W.; Wardle, M.; Tatischeff, V.; Roberts, D.; Cotton, W.; Uchiyama, H.; Nobukawa, M.; Tsuru, T. G.; Heinke, C. et al. Interacting Cosmic Rays with Molecular Clouds: A Bremsstrahlung Origin of Diffuse High Energy Emission from the Inner 2deg by 1deg of the Galactic Center. *Astrophys. J.* **2013**, *762*, 1-33
- (43) LaRosa, T. N.; Brogan, C. L.; Shore, S. N.; Lazio, T. J.; Kassim, N. E.; Nord, M. E. Evidence of a Weak Galactic Center Magnetic Field from Diffuse Low-Frequency Nonthermal Radio Emission. *Astrophys. J.* **2005**, *626*, L23-L27
- (44) Egan, M. P.; Shipman, R. F.; Price, S. D.; Carey, S. J.; Clark, F. O.; Cohen, M. A Population of Cold Cores in the Galactic Plane. *Astrophys. J.* **1998**, *494*, L199
- (45) Price, S. D.; Egan, M. P.; Carey, S. J.; Mizuno, D. R.; Kuchar, T. A. Midcourse Space Experiment Survey of the Galactic Plane. *Astron. J.* **2001**, *121*, 2819-2842
- (46) Rodriguez-Fernandez, N. J.; Martin-Pintado, J.; Fuente, A.; de Vicente, P.; Wilson, T.L.; Hüttemeister, S. Warm H<sub>2</sub> in the Galactic Center Region. *Astron. Astrophys.* **2001**, *365*, 174-185
- (47) Simpson, J. P.; Colgan, S. W. J.; Cotera, A. S.; Erickson, E. F.; Hollenbach, D. J. Warm H<sub>2</sub> in the Galactic Center Region. *Astrophys. J.* **2007**, *670*, 1115-1131
- (48) Oka, T.; Hasegawa, T.; Sato, F.; Tsuboi, M.; Miyazaki, A. A Molecular Cloud and an Expanding Cavity Adjacent to the Nonthermal Filaments of the Galactic Center Radio Arc. *Publ. Astron. Soc. Jpn.* **2001**, *53*, 779-786
- (49) Schöier, F.L.; van der Tak, F.F.S.; van Dishoeck E.F.; Black, J.H. An Atomic and

- Molecular Database for Analysis of Submillimetre Line Observations. *Astron. Astrophys.* **2005**, *432*, 369-379
- (50) Neufeld, D. A.; Kaufman, M. J. Radiative Cooling of Warm Molecular Gas. *Astrophys. J.* **1993**, *418*, 263
- (51) Neufeld, D. A.; Lepp, S.; Melnick, G. J. Thermal Balance in Dense Molecular Clouds: Radiative Cooling Rates and Emission-Line Luminosities. *Astrophys. J. Supp* **1995**, *100*, 132
- (52) Glassgold, A.; Galli, D.; Padovani, M. Cosmic-Ray and X-Ray Heating of Interstellar Clouds and Protoplanetary Disks. *Astrophys. J.* **2012**, *756*, 157
- (53) Kulsrud, R.; Pearce, W. P. The Effect of Wave-Particle Interactions on the Propagation of Cosmic Rays. *Astrophys. J.* **1969**, *156* 445
- (54) Zweibel, E. G.; Josafatsson, K. Hydromagnetic Wave Dissipation in Molecular Clouds. *Astrophys. J.* **1983**, *270*, 511-518
- (55) van der Tak, F. F. S.; Black, J. H.; Schöier, F. L.; Jansen, D. J.; van Dishoeck, E. F. A Computer Program for Fast Non-LTE Analysis of Interstellar Line Spectra. With Diagnostic Plots to Interpret Observed Line Intensity Ratios. *Astron. Astrophys.* **2007**, *468*, 627-635
- (56) Geppert, W. D.; Hamberg, M.; Thomas, R. D.; Osterdahl, F.; Hellberg, F.; Zhaunerchyk, V.; Ehlerding, A.; Millar, T. J.; Roberts, H.; Semaniak, J. et al. Dissociative recombination of protonated methanol *Chemical Evolution of the Universe, Faraday Discussions* **2006**, *133*, 177-190
- (57) Viti, S.; Jimenez-Serra, I.; Yates, J. A.; Codella, C.; Vasta, M.; Caselli, P.; Lefloch, B.;



- Ceccarelli, Water and Ammonia as Diagnostics of Shock Temperature. *Astrophys. J.* **2011**, *740*, L3-5
- (58) Roberts, J. F.; Rawlings, J. M. C.; Viti, S. & Williams, D. A. Desorption from Interstellar Ices. *Mon. Not. R. Astron. Soc.* **2007**, *382*, 733-742
- (59) Minh, Y. C.; Irvine, W. M. & Friberg, P. Molecular Abundances in the Sagittarius A Molecular Cloud. *Astron. & Astrophys.* **1992**, *258*, 489-494
- (60) Martin-Pintado, J.; de Vicente, P.; Fuente, A. & Planesas, P. SiO Emission from the Galactic Center Molecular Clouds. *Astrophys. J.* **1997**, *482*, L45-L48
- (61) Martin-Pintado, J.; Rizzo, J. R. de Vicente, P.; Rodriguez-Fernandez, N. J. & Fuente, A. & Planesas, P. Large-Scale Grain Mantle Disruption in the Galactic Center. *Astrophys. J.* **2001**, *548*, L65-L68
- (62) Kimura, Hiroshi; Mann, Ingrid; Jessberger, Elmar K. Elemental Abundances and Mass Densities of Dust and Gas in the Local Interstellar Cloud *Astrophys. J.* **2003**, *582*, 846-858
- (63) Sofia, U. J.; Meyer, D. M. Interstellar Abundance Standards Revisited. *Astrophys. J.* **2001**, *554*, L221-L224
- (64) Sofia, U. J.; Cardelli, J. A.; Savage, B. D. The Abundant Elements in Interstellar Dust. *Astrophys. J.* **1994**, *430*, 650-666

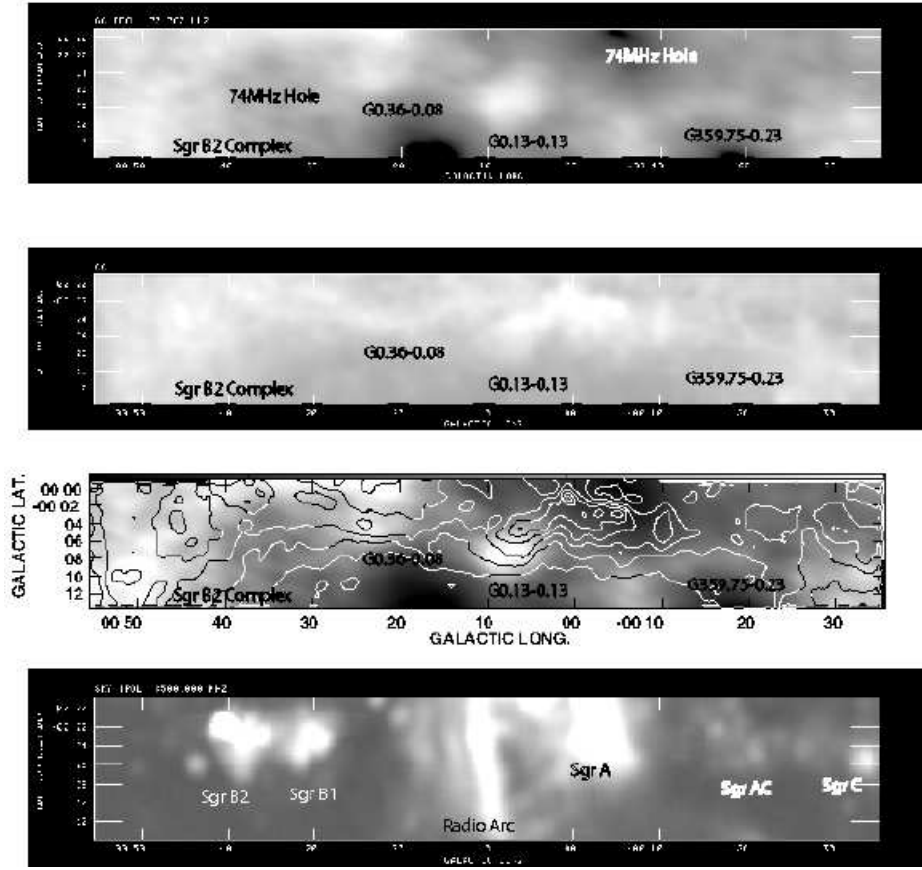


Fig. 1.— (Top to Bottom) (a) A grayscale 74 MHz distribution of the inner  $1.5^\circ \times 12'$  (Galactic coordinates  $l \times b$ ) convolved to a resolution of  $2' \times 2'$  based on VLA observations. The 74 MHz flux range is between -1 and 4 Jy. (b) Similar to (a) except the distribution of CO (3-2) integrated over  $\pm 200 \text{ km s}^{-1}$  at  $34''$  resolution<sup>48</sup> with flux range 100 and 2500  $\text{km s}^{-1} \text{ K}$ . (c) Contours of the CO (3-2) line emission shown in (b) are superimposed on the 74 MHz image shown in (a). (d) Similar to (a) except observed with the GBT at 8.5 GHz with a resolution of  $88''$ <sup>34</sup>. The flux range is between  $-5\text{e-}3$  and 0.4 Jy.

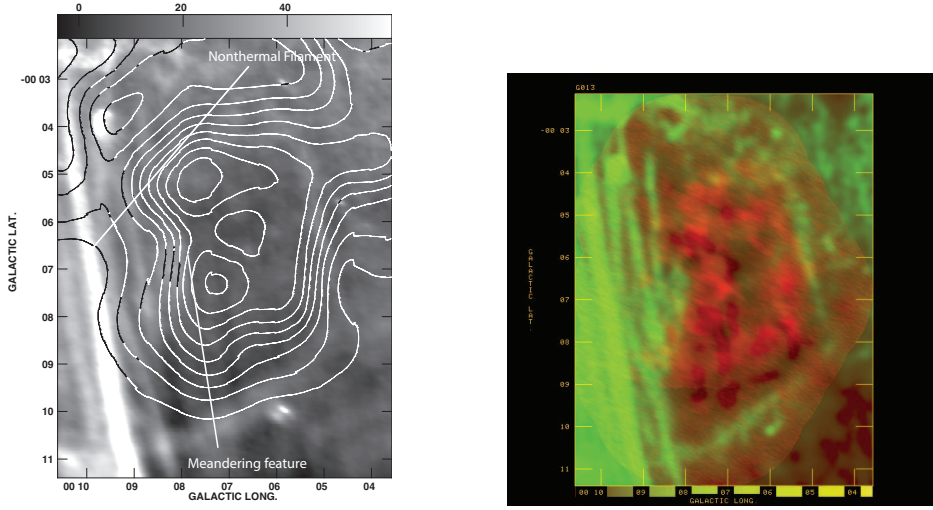


Fig. 2.— *(a - Left)* Contours of CS (1-0) line emission integrated between 0 and 50 km s<sup>-1</sup> from the G0.13–0.13 molecular cloud with a resolution of 45''<sup>25</sup> are superimposed on a 5 GHz continuum image with a spatial resolution of 10.8'' × 5.5'' (PA=-2.6°). Contour levels are set at 2 to 10 km s<sup>-1</sup> K (T<sub>A</sub><sup>\*</sup>) with 1 km s<sup>-1</sup> K interval. *(b - Right)* The distribution of CS (2-1) line emission (red) from G0.13–0.13 integrated over velocities between -12.1 < v<sub>LSR</sub> < 76.4 km s<sup>-1</sup> with a resolution of 3.1'' × 2.6'' (PA=20.5°) is based on BIMA observations. The extended nonthermal filaments of the Arc at 1.4 GHz with a resolution of 10.7'' × 10.1'' (PA=28°) are shown in green.

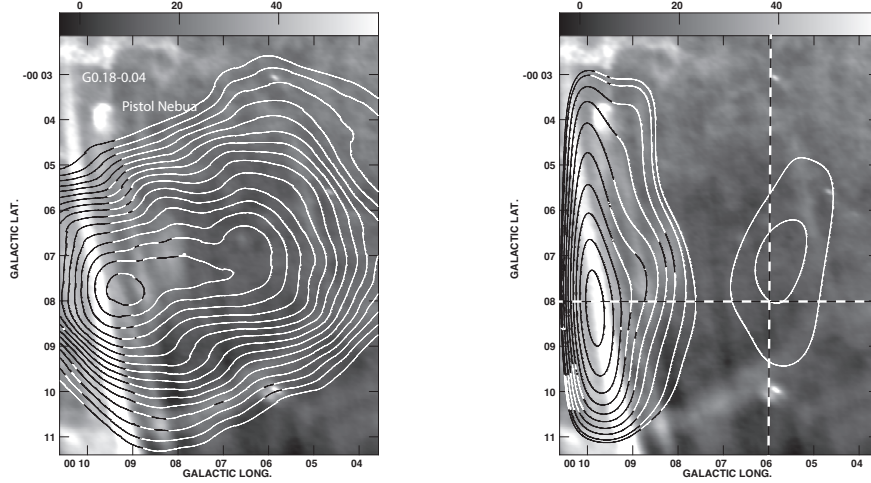


Fig. 3.— *(a - Top Left)* Contours of 74 MHz emission with a resolution  $122'' \times 64''$  ( $PA = -5^\circ$ ) with levels set at 0.8, 0.9, ... 2.3  $\text{Jy beam}^{-1}$  are superimposed on a grayscale image at 5 GHz. *(b - Top Right)* Contours of 327 MHz emission with levels  $(0.8, 0.9, \dots 2.3) \times 2$  are shown with the same resolution as in (a) and are superimposed on the 5 GHz image. The white dashed lines show the location of cross cuts (see (d) below). *(c - Left)* The spectral index distribution  $\alpha$  between 74 and 327 MHz emission. The 74 and 327 MHz are convolved to the same resolution and are background subtracted by 2 and 0.5 Jy, respectively. The bar at the bottom of the figure shows the color scale version of spectral index values ranging between -0.5 and 2 (see text). *(d-e - Right)* Top two panels show background subtracted intensity profiles at 327 and 74 MHz (top) and the corresponding spectral index distribution between these two frequencies (below) made from vertical latitude cross cut at constant longitude  $l = -6'$ , as drawn on (b) with a vertical dashed line. Bottom two panels are the same as the top two panels except that the cross cuts made horizontally at constant  $b = -8'$ . Cross cuts are made on the 74 and 327 MHz images.

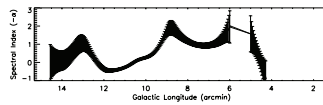
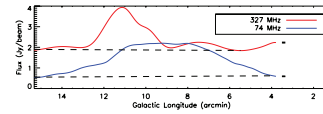
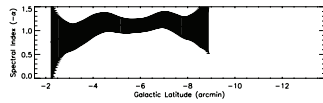
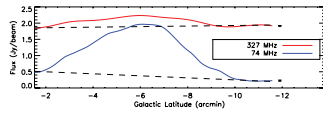
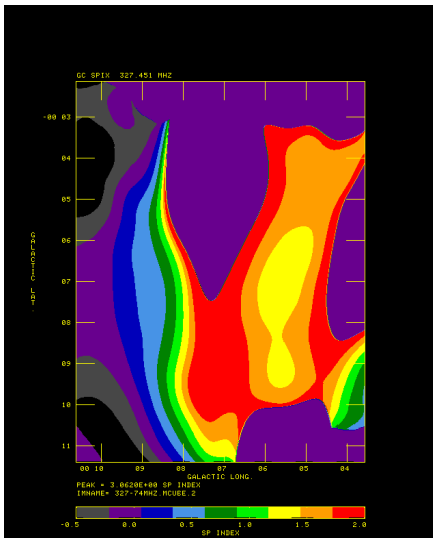


Fig. 3.— continued

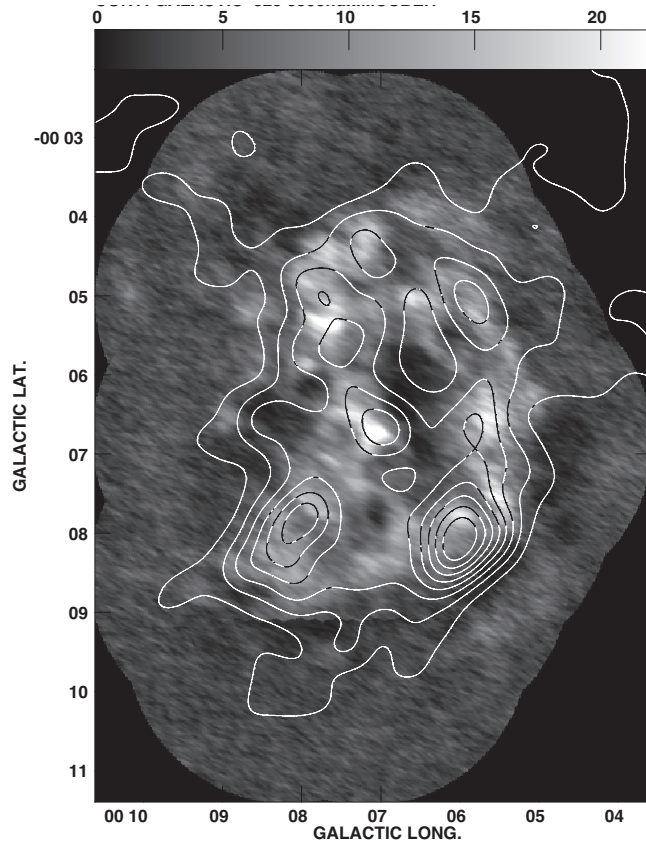


Fig. 4.— Contours of  $K\alpha$  line emission at 6.4 keV line emission at  $(2, 3, \dots, 9) \times 10^{-6}$   $\text{ph s}^{-1} \text{cm}^{-2} \text{beam}^{-1}$  are superimposed on a CS (1-0) line emission, as shown in Figure 2b. CARMA image shows emission between 6.25 and 6.5 keV which is convolved to a Gaussian beam of  $30''$ .

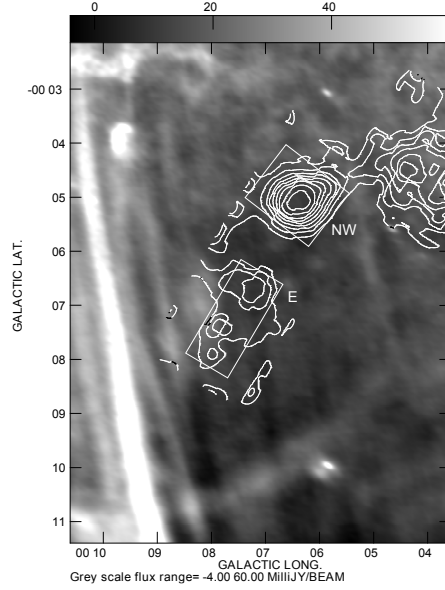


Fig. 5.— (a) Contours of SiO (5-4) line emission integrated between  $-20$  and  $100 \text{ km s}^{-1}$  with levels at  $8, 10, 12, 14, 16, 18, 20, 23 \text{ K km s}^{-1}$  ( $T_{\text{mb}}$  velocity) are superimposed on a  $5 \text{ GHz}$  grayscale image. Two rectangular boxes NW and E are drawn for LVG analysis. (b) The parameters of density  $n_{\text{H}} \text{ cm}^{-3}$  and temperature  $T$  (K) using LVG model are presented. SiO (5-4), (6-5), (2-1) line ratios are displayed in the bottom left corner in red, green and black, respectively. The dashed lines show the corresponding calibration uncertainties of the derived parameters at a level of 25%. The SiO line intensity ratios are extracted from the region presented by the E rectangular box, as drawn schematically on (a). (c) Similar to (b) except that data are from the NW box shown in (a). (d) Top three panels show the plots of line ratios as function of logarithm of pressure ( $nT$ ) based on a grid of models. The observed line ratio values with their corresponding errors are drawn horizontally (green) in solid and dashed lines, respectively. The bottom panel shows the best  $\chi^2$  fit to the grid of models. The vertical lines (green) are centered near minimum  $\chi^2$  giving  $\log(nT)$  values in the range of 6.4–6.9.

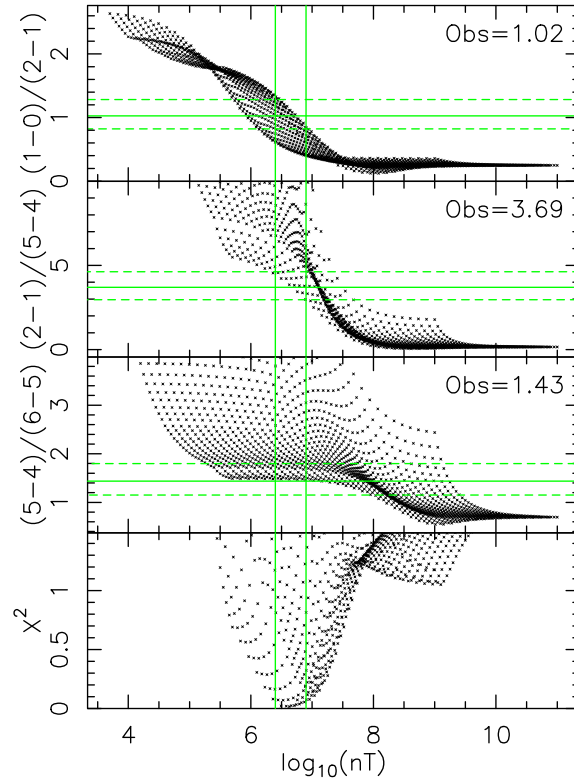
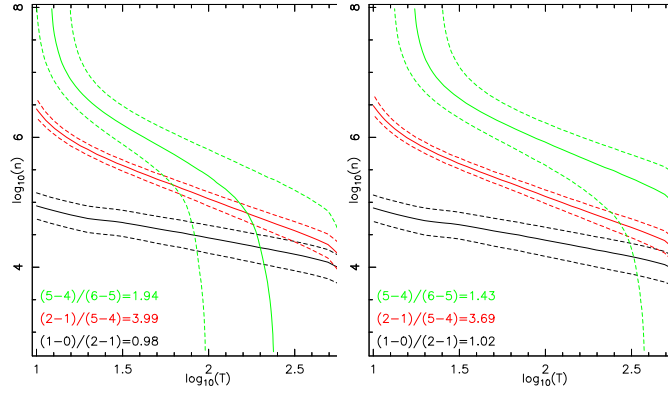


Fig. 5.— continued



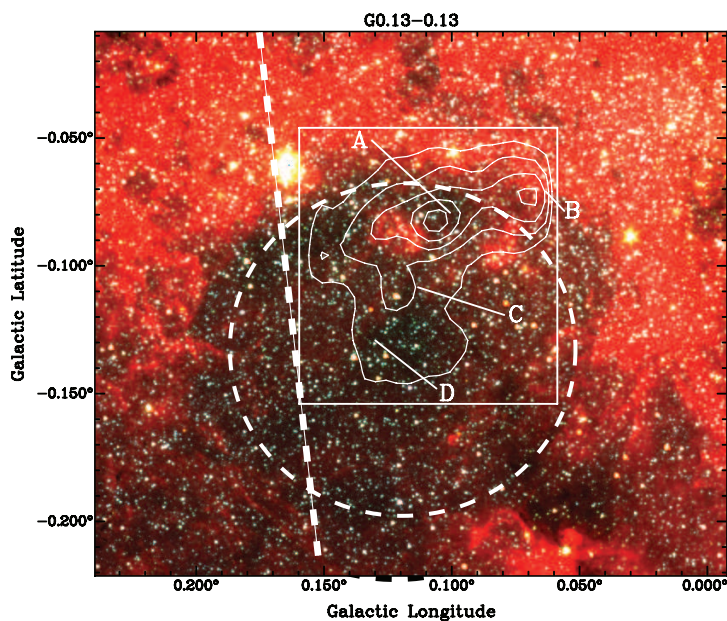


Fig. 6.— Contours of SiO (2-1) line emission based on Mopra observations with levels 2, 3.5, 5, 6.5, 8 K km s<sup>-1</sup> are superimposed on a three color Spitzer/IRAC image combining Channels 4 (8 $\mu$ m) is red), 2 (4.5 $\mu$ m) is green and 1 (3.6 $\mu$ m) is blue. The temperature scale is in T<sub>A</sub><sup>\*</sup>. The straight line in white shows the orientation of the nonthermal filament of the radio arc whereas the dashed circle marks roughly the size of the arc bubble. The positions where molecular abundances are measured are drawn as A, B, C and D. The box indicated the region mapped by Mopra.

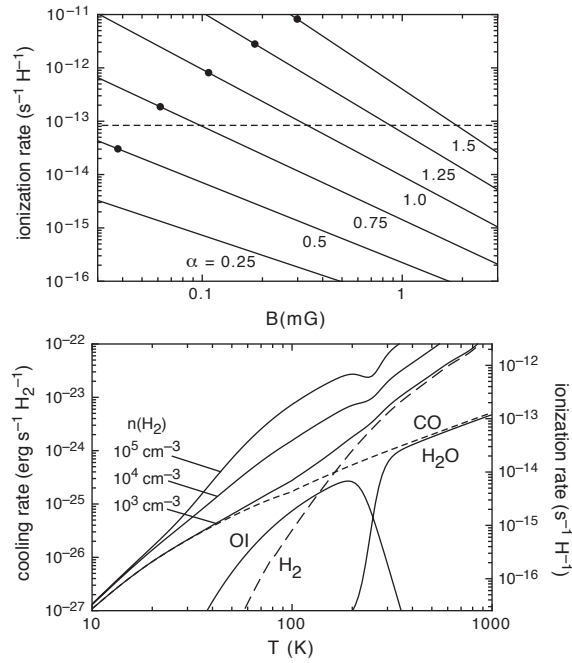


Fig. 7.— (a - Top) The variation of cosmic ray ionization rate as a function of magnetic field strength for different values of the spectral index of the radiation  $\alpha$ . The black dot on each curve gives the value at which the magnetic field and particle energies are in equipartition. (b - Bottom) Solid curves show the total cooling rate for diffuse molecular gas for H<sub>2</sub> densities of 10<sup>3</sup>, 10<sup>4</sup> and 10<sup>5</sup> cm<sup>-3</sup>. Rotational transitions of H<sub>2</sub>, CO and H<sub>2</sub>O, and by fine-structure transitions of OI have been included; their individual contributions for 10<sup>3</sup> cm<sup>-3</sup> are indicated by the dashed curves. The right hand axis shows the ionization rate by cosmic-ray electrons needed to supply the corresponding heating rate (see text). The vertical axis in both figures are logarithmic.

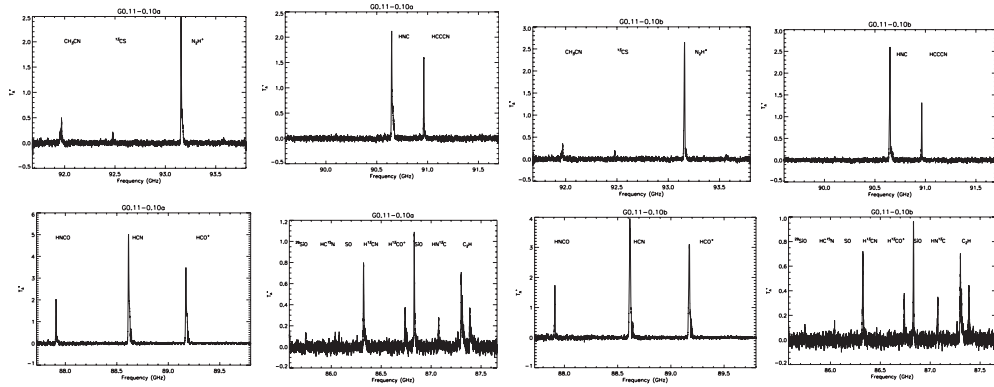


Fig. 8.— (*a - Top Left 4*) Deep pointed observations showing the spectra of 16 molecules toward position A in G0.13–0.13 (*b - Top Right 4*) Similar to (*a*) except for position B. (*c - Top Left 4*) Similar to (*a*) except for position C. (*d - Top Right 4*) Similar to (*a*) except for position D.

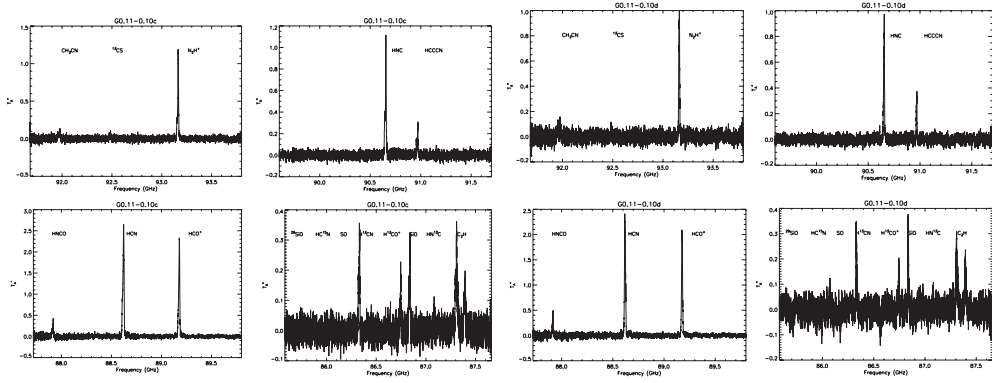


Fig. 8.— continued

Table 1. Observed Positions within G0.13–0.13

| Source | $\ell$         | $b$            |
|--------|----------------|----------------|
| Name   | [ $^{\circ}$ ] | [ $^{\circ}$ ] |
| A      | 0.1007         | -0.0792        |
| B      | 0.0632         | -0.0709        |
| C      | 0.1132         | -0.1084        |
| D      | 0.1299         | -0.1292        |

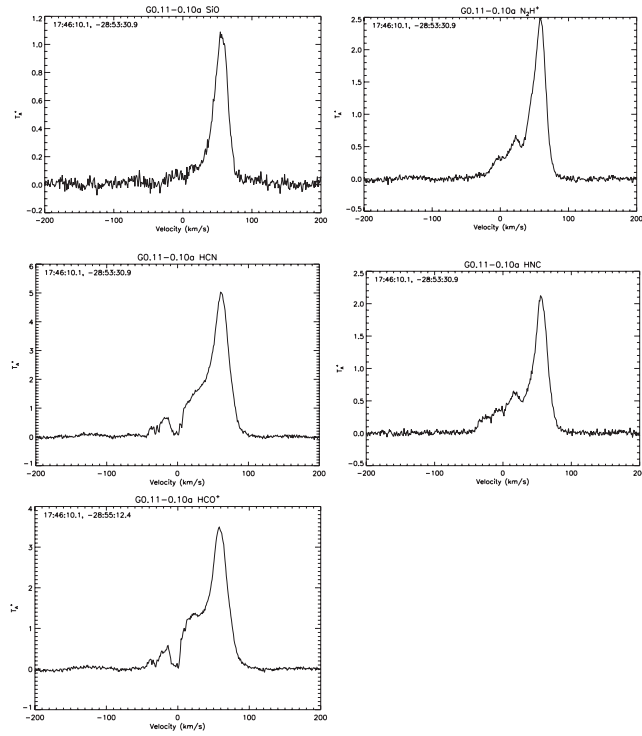


Fig. 9.— Individual spectrum of five molecular species  $\text{SiO}$ ,  $\text{HCN}$ ,  $\text{HNC}$ ,  $\text{HCO}^+$  and  $\text{N}_2\text{H}^+$  toward position A based on Mopra observations.

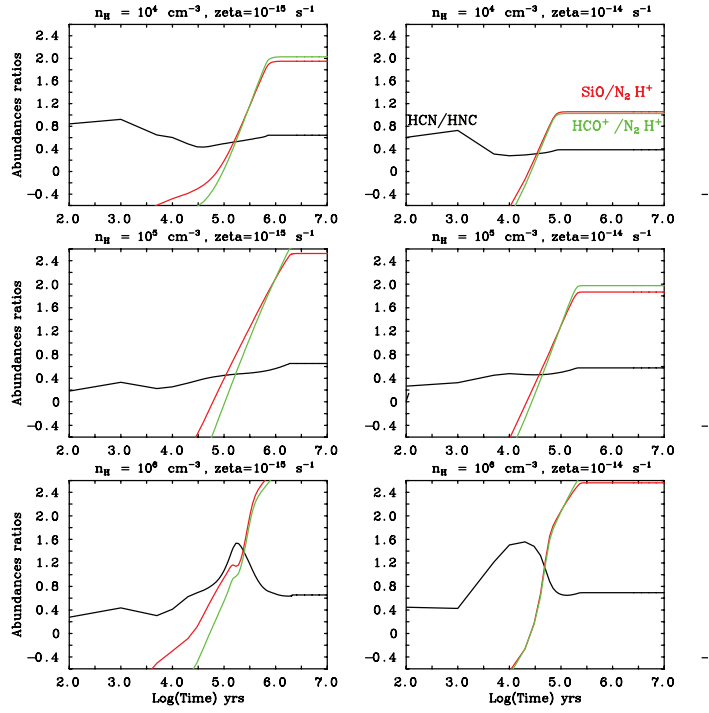


Fig. 10.— Abundance ratios of HCN/HNC (black) and HCO<sup>+</sup>/N<sub>2</sub>H<sup>+</sup> (green) and SiO/N<sub>2</sub>H<sup>+</sup> (red) as a function of time in years for different values of cosmic ray ionization rate and molecular gas density. The chemical evolution of the G0.13–0.13 cloud uses the UCL\_CHEM time-dependent gas-grain chemical model<sup>31</sup>. Using the same color scheme in the model, the observed abundance ratios for all four positions A-D are marked on the top right panel.

Table 2. Observed Peak Line Intensities, LSR Velocities and their  $1\sigma$  Errors

| Source<br>Name | $v_1(\text{HCN})$<br>km s <sup>-1</sup> | $T_A^*(\text{HCN})$<br>Peak (K) | $v(\text{HCO}^+)$<br>km s <sup>-1</sup> | $T_A^*(\text{HCO}^+)$<br>Peak (K) | $v(\text{HNC})$<br>km s <sup>-1</sup> | $T_A^*(\text{HNC})$<br>Peak (K) | $v(\text{N}_2\text{H}^+)$<br>km s <sup>-1</sup> | $T_A^*(\text{N}_2\text{H}^+)$<br>Peak (K) | $v(\text{SiO})$<br>km s <sup>-1</sup> | $T_A^*(\text{SiO})$<br>Peak (K) |
|----------------|---|---------------------------------|---|-----------------------------------|---------------------------------------|---------------------------------|---|---|---------------------------------------|---------------------------------|
| A              | 60.65±0.9                               | 5.02±0.03                       | 57.91±0.90                              | 3.49±0.03                         | 54.92±0.90                            | 2.12±0.02                       | 58.13±0.90                                      | 2.49±0.02                                 | 54.29±0.90                            | 1.09±0.03                       |
| B              | 57.88±0.90                              | 3.96±0.03                       | 51.53±0.90                              | 3.10±0.03                         | 50.42±0.90                            | 2.59±0.02                       | 48.54±0.90                                      | 2.64±0.03                                 | 49.60±0.90                            | 0.96±0.03                       |
| C              | 34.19±0.90                              | 2.65±0.03                       | 34.33±0.90                              | 2.33±0.03                         | 28.15±0.90                            | 1.12±0.03                       | 32.08±0.90                                      | 1.19±0.02                                 | 26.36±0.90                            | 0.32±0.02                       |
| D              | 32.35±0.90                              | 1.98±0.03                       | 41.56±0.90                              | 1.98±0.03                         | 30.81±0.90                            | 0.97±0.03                       | 33.80±0.90                                      | 1.00±0.03                                 | 42.1±0.90                             | 0.38±0.03                       |

Table 3. Predicted Column Density from Observed Intensity Ratios

| Source | $[N(\text{HCN})]/[N(\text{HNC})]$ | $[N(\text{HCO}^+)/N(\text{N}_2\text{H}^+)]$ | $[N(\text{SiO})/N(\text{N}_2\text{H}^+)]$ | $T_A^*(\text{HCN})/T_A^*(\text{HNC})$ | $T_A^*(\text{HCO}^+)/T_A^*(\text{N}_2\text{H}^+)$ | $T_A^*(\text{SiO})/T_A^*(\text{N}_2\text{H}^+)$ |
|--------|-----------------------------------|---|---|---------------------------------------|---|---|
| A      | $0.33 \pm 0.01$                   | $0.13 \pm 0.01$                             | $-0.10 \pm 0.01$                          | $2.37 \pm 0.03$                       | $1.40 \pm 0.02$                                   | $0.44 \pm 0.01$                                 |
| B      | $0.01 \pm 0.001$                  | $0.005 \pm 0.001$                           | $-0.20 \pm 0.02$                          | $1.53 \pm 0.02$                       | $1.17 \pm 0.02$                                   | $0.36 \pm 0.01$                                 |
| C      | $0.35 \pm 0.005$                  | $0.19 \pm 0.01$                             | $-0.41 \pm 0.03$                          | $2.37 \pm 0.05$                       | $1.96 \pm 0.04$                                   | $0.27 \pm 0.02$                                 |
| D      | $0.26 \pm 0.01$                   | $0.16 \pm 0.01$                             | $-0.24 \pm 0.03$                          | $2.04 \pm 0.06$                       | $1.98 \pm 0.07$                                   | $0.38 \pm 0.03$                                 |